Journal of Materials Chemistry A

Sodium Trithiocarbonate Cathode for High-Performance Sodium-Sulfur Batteries

Journal:	*Journal of Materials Chemistry A*
Manuscript ID	TA-ART-10-2022-007918.R1
Article Type:	Paper
Date Submitted by the Author:	23-Nov-2022
Complete List of Authors:	Sul, Hyunki; The University of Texas at Austin Bhargav, Amruth; The University of Texas at Austin Manthiram, Arumugam; The University of Texas at Austin, Materials Science and Engineering

ARTICLE

Sodium Trithiocarbonate Cathode for High-Performance Sodium-Sulfur Batteries

Received 00th January 20xx,
Accepted 00th January 20xx

DOI: 10.1039/x0xx00000x

Hyunki Sul [a], Amruth Bhargav [a] and Arumugam Manthiram*[a]

The high abundance and low cost of sodium and sulfur make room-temperature sodium-sulfur (RT Na-S) batteries an attractive technology compared to the current lithium-ion batteries for large-scale grid-storage applications. However, the commercialization of RT Na-S batteries is impeded by the slow kinetics of Na-S chemistry, severe sodium polysulfide shuttling, and uncontrollable growth of dendritic Na. Herein, sodium trithiocarbonate (Na_2CS_3) is applied as a cathode material to facilitate concurrent improvement in both electrodes, leading to a high-rate performance with extended cycle life. The conductive characteristic of the carbon-sulfur resonance bond provides fast ion and electron transfer throughout the cathode, resulting in superior electrochemical reactivity. At the cathode, the presence of Na_2CS_3 forms an oligomer-structured layer to suppress the dissolution and shuttling of active materials. Meanwhile, when small portions of Na_2CS_3 intermediates migrate to the anode, a stable solid electrolyte interphase (SEI) layer with uniform Na-ion flux is formed, enabling improved Na stripping and plating performance. A series of electrochemical and materials characterization, accompanied by density functional theory calculations demonstrate that Na_2CS_3 is a promising candidate to realize high-rate performance long cycle life RT Na-S batteries.

Introduction

The rapid growth in global energy demand drives the development of clean energy technologies with sustainable sources, such as wind and solar energies. To resolve the challenges coming from the intermittence of these renewable energy sources, secondary Li-ion battery technologies have become one of the most attractive strategies.[1-4] However, the intrinsic barriers of traditional Li-ion batteries, including limited energy density to < 250 W h kg^{-1} and less abundant resources of some elements[5] hinder their use to large-scale applications. Among various alternative energy storage systems, metal-sulfur batteries have become a promising strategy due to their high energy density, low cost, and high natural abundance.[6] Especially, sodium-sulfur (Na-S) electrochemistry is gaining attention since it delivers a high theoretical energy density of 1274 W h kg^{-1} while the price of sodium is only 1/25 of that of lithium (Li : 20 mg kg^{-1} vs. Na : 23,600 mg kg^{-1} in the earth crust).[7]

The history of Na-S batteries dates back to the 1960s, when the molten states of sodium and sulfur (operating at a temperature range of 300 – 350 °C) were proposed and developed for stationary energy-storage applications.[8–10] However, the high operating temperatures and the reactive nature of Na and S in their molten state cause severe durability, safety, and maintenance issues.[11] Hence, room-temperature Na-S (RT Na-S) battery systems have been pursued over the past decade as a promising alternative for both stationary grid storage and transportation applications.

RT Na-S batteries were introduced in 2006 with high capacity and well-defined charge / discharge curves,[12] but they suffer from poor cycling stability. Similar to lithium-sulfur (Li-S) batteries, the critical challenge is the intrinsic soluble behavior of the intermediate charge / discharge species, the so-called sodium polysulfides, in liquid electrolytes.[13,14] Although the chemistries of Na-S and Li-S are analogous, the more reactive characteristic of Na metal and the extreme solubility of sodium polysulfides in liquid electrolytes aggravates capacity fade. Long-chain glyme-based ethers, such as tetraethylene glycol dimethyl ether (TEGDME), have been considered as promising electrolytes because of their high boiling point and good electrochemical stability towards polysulfide anions.[15–17] Nevertheless, fast capacity decay is still encountered as the dissolved sodium polysulfides freely shuttle between the cathode and the anode. The migrated sodium polysulfides spontaneously react with Na metal and get reduced into insulating Na_2S, leading to a loss of active lithium and sulfur species.

Furthermore, Na metal with a highly reducing nature can undergo irreversible reaction with solvent molecules or salts that leads to a loss of Na inventory and depletion of the electrolyte. Above all, conventional RT Na-S batteries could not maintain a stable solid-electrolyte interface (SEI) that would prevent the degradation of the Na-metal anode.[18] Accordingly, preventing sodium polysulfide shuttling and protecting Na-metal anode have been the critical strategies for extending the cycle life and improving the performance of RT Na-S batteries.

[a] *Walker Department of Mechanical Engineering, The University of Texas at Austin, Austin, TX 78712, United States*

† Electronic Supplementary Information (ESI) available. See DOI: 10.1039/x0xx00000x

One of the most promising solutions to mitigate the long-chain sodium polysulfide shuttling is adsorption and immobilization of the polysulfide species. Strong polysulfide adsorption sites could effectively confine the sodium polysulfides in the cathode side and reduce the shuttle effect. Metal-based sulfiphilic sites are known to effectively immobilize the polysulfides.[19–21] Metals, such as Ti, Mn, and Cu, polarize the cathode surface and provide strong polysulfide adsorption ability through polar-polar interactions. Other inorganic compounds, such as MXenes, have also been reported as promising materials owing to their outstanding polysulfide immobilization ability and high areal sulfur loading.[22] Another promising strategy is to utilize electrocatalysts to promote a facile conversion of long-chain polysulfides into insoluble short-chain polysulfides, which precipitate out and remain on the cathode side. Transition metal-based electrocatalysts (Co, Fe, Cu, and Ni) combined with carbon hosts have been reported to be effective in facilitating fast electrochemical kinetics for sodium polysulfide redox reaction.[23–26] Thus, the aforementioned strategies, including the adsorption and conversion of the long-chain polysulfides, are well-known strategies to prevent the dissolution and migration of polysulfides.

To overcome the challenges of reactive Na-metal anode degradation, the importance of homogeneous Na surface morphology control has been emphasized. The formation of a smooth and dense Na surface minimizes the reaction sites that can undergo parasitic reactions with the electrolyte and polysulfides. It is well known that the chemical composition of the SEI layer critically impacts the Na morphology since Na ions are plated onto and stripped from the underlying Na metal during cycling. The stripping and plating of Na metal takes place through the following steps: (1) electron transfer at bulk Na metal / SEI interface; (2) diffusion of Na ions through the SEI layer; and (3) Na-ion transfer at SEI / electrolyte interface.[27,28] Based on various experimental results, step 2 is recognized as the rate-determining step that controls the nucleation and morphology of Na-metal anode. Therefore, the formation of a kinetically favorable SEI layer with uniform Na-ion flux is crucial in facilitating a homogeneous Na deposition. Artificial SEI layers, including NaBr, Na_xSn_y, and ionic polymers, have been introduced to reduce the Na-ion diffusion barrier.[29–31] Electrolyte additives to modify the physical and chemical properties of the SEI layers have also been reported.[32–34]

Recently, some reports have shown that trithiocarbonates enhance the cycling performance of Li-S batteries by simultaneously stabilizing both the cathode and the anode sides.[35-37] In this work, inspired by the outstanding performance of trithiocarbonates in Li-S systems, sodium trithiocarbonate (Na_2CS_3) was synthesized and applied as a cathode material to improve the electrochemical performance of RT Na-S cells. Evidence from experimental results and theoretical calculations indicates several intriguing characteristics: (i) The highly covalent character of Na_2CS_3 molecules provide an efficient electron and ion conductive network, which improves the utilization of active materials and rate performance. (ii) Oligomer-structured intermediates formed upon cell charge have less tendency to dissolve into the electrolyte, thus reducing the polysulfide shuttle effect. (iii) A unique composition of SEI is formed on the Na-metal surface, facilitating a uniform Na-ion flux and homogenous Na morphology. The half cells with Na_2CS_3 cathode show remarkable improvements in their initial discharge capacity and cycling performance (55 % retention after 100 cycles) compared to the Na_2S cathode (14 % retention after 100 cycles). A series of material characterization methodologies support the notion that trithiocarbonate is applicable in the Na-S system, and it has enormous potential for high-energy-density, long cycle life RT Na-S batteries.

Experimental

Synthesis and preparation of Na_2CS_3 and Na_2S cathode

Na_2CS_3 was synthesized by a simple one-step wet ball-milling method. Commercial sodium sulfide powder (Na_2S, Sigma Aldrich) was initially refined with zirconia (YSZ) grinding media in a zirconia milling container at 400 rpm. The total milling duration was 24 h with intervals of 30 min milling followed by 30 min resting. The refined Na_2S powder and carbon disulfide (CS_2, Alfa Aesar) were transferred into a PTFE bottle in a 1 : 3 mole ratio. 15 mL of 1,2-dimethoxyethane (DME) was added as a slurry medium and zirconia ceramic balls were used as a grinding media. The slurry was wet ball milled for 24 h with a long roll jar milling apparatus (US Stoneware 802 CVM). The resulting slurry was dried at 50 °C for 2 h to remove the solvents and obtain Na_2CS_3 powder.

Na_2CS_3 cathodes were prepared by wet ball-milling the synthesized Na_2CS_3 powder and commercial multi-walled carbon nanotubes (MWCNT, Nanostructured & Amorphous Materials Inc.) in a 7 : 3 weight ratio. The homogeneously mixed slurry was drop casted between two pieces of carbon nanotube papers (AvCarb P50, 7/16-inch diameter) and fully dried to make a binder-free Na_2CS_3 cathode. The loading of Na_2CS_3 in the cathode is 1.5 mg cm^{-2} or 3.0 mg cm^{-2}.

Binder-free Na_2S cathodes were obtained with an analogous procedure. The refined Na_2S powder was wet ball milled with MWCNT in a 7 : 3 weight ratio for 24 h. The slurry was then drop casted into carbon nanotube papers at a Na_2S loading of 1.5 mg cm^{-2} or 3.0 mg cm^{-2}.

Materials characterization

X-ray diffraction (XRD) was performed with a Rigaku Miniflex 600 diffractometer. XRD patterns were collected at a scan rate of 0.5° min^{-1} with a step size of 0.02°. Fourier transform infrared spectra (FTIR) were collected with a Thermo Scientific Nicolet iS5 FTIR spectrometer. Nuclear magnetic resonance (NMR) spectroscopy was performed with a Bruker Avance III 500 MHz NMR spectrometer. D_6-Acetone was used as a solvent media. X-ray photoelectron spectroscopy (XPS) measurements were carried out with a Kratos Analytical spectrometer with a monochromatic Al Kα as a radiation

source. The data processing and peak fitting were conducted with the CasaXPS software. The surface morphologies of the synthesized materials and electrodes were examined with a FEI Quanta 650 field emission scanning electron microscope (SEM). Thermogravimetric analysis (TGA) was conducted with Mettler TGA/DSC 1 in an argon atmosphere. The temperature ramp rate was 10 °C min^{-1}. Ultraviolet-visible (UV-Vis) spectroscopy data were collected with a Cary 5000 spectrophotometer.

Electrochemical cell assembly

Na metal half cells were assembled in CR-2032-type coin cells inside an argon-filled glovebox. The cells consist of Na-metal foil anode, 1.5 M sodium perchlorate ($NaClO_4$) and 0.2 M sodium nitrate ($NaNO_3$) in tetraethylene glycol dimethyl ether (TEGDME) electrolyte, ceramic coated Celgard separator, and binder-free cathodes. The cells contained active material loadings of 1.5 mg cm^{-2} or 3.0 mg cm^{-2} with an electrolyte to an active material ratio of 25 µL mg^{-1}. The Na ll Na symmetric cells were assembled with an identical Na metal foil as a working and counter electrode and the abovementioned electrolyte.

Electrochemical performance measurements

The electrochemical cell cycling was conducted with an Arbin battery cycler at room temperature. A voltage window of 1.2 to 2.6 V was employed at a C/10 rate. The stability of the symmetric cells was evaluated at a current density of 1 mA cm^{-2} and an areal capacity of 1 mA h cm^{-2}. Cyclic voltammetry (CV) data was collected with a Biologic VMP potentiostat at a rate of 0.05 mV s^{-1}. The electrochemical impedance spectroscopy (EIS) measurements were performed with a Biologic VMP potentiostat at a frequency of 1 MHz to 0.1 kHz.

Optical H-type cell assembly

In-situ visible electrochemical tests were conducted in an H-type glass cell. The H-type cell was tested inside a glovebox within a voltage range of 1.2 to 2.6 V with a VoltaLab potentiostat. 7.7 mg of active material was uniformly drop-casted onto a CNT paper and dried overnight to obtain the binder-free cathodes. The cathodes were combined with Na metal foil and cycled at a low current of 40 µA.

Density functional theory-based calculations

To evaluate the electron density distribution and electronic conductivity of the molecules, first principle-based calculations were conducted with the Vienna ab initio simulation package (VASP). The generalized gradient approximation (GGA) with Perdew-Burke-Ernzerhof (PBE) correlation functional was used as a baseline theory.[38,39] An energy cutoff of 600 eV was applied with a Monkhorst-Pack reciprocal space grid of 2 x 2 x 2. The molecular structures were prepared with Avogadro 1.2.0 software and relaxed until the residual force on the entire system is below 0.02 eV. The density of states (DOS) was calculated with the Heyd-Scuseria-Erznerhof functional. The average net charge was calculated with Bader charge analysis F90 open-source code.

Results and discussion

Synthesis and material characterization

Na_2CS_3 has been reported as an effective precipitating agent to remove heavy metals from galvanic wastewater for decades.[40,41] Trithiocarbonates can be easily formed from a reaction between carbon disulfide (CS_2) and other sulfide sources.[42-44] Here, the synthesis of Na_2CS_3 was carried out by a one-step wet ball milling of sodium sulfide (Na_2S), and an excess amount of CS_2 in a mole ratio of 1 : 3. 1,2-dimethoxyethane (DME) was used as the slurry medium to facilitate a homogenous reaction between solid Na_2S and liquid CS_2 (Figure 1a). After drying out the solvent and surplus CS_2, the orange-red colored powder was collected. The scanning electron microscopy (SEM) image of the synthesized product reveals the surface morphology change from granular micron-sized (2 – 8 µm) Na_2S to the largely clustered (20 µm) compound, which indicates the chemical transformation taking place at the surface (Figure S1). The bulk crystalline structure of the obtained compound was examined with X-ray diffraction (XRD), as shown in Figure 1b. Kapton tape was used to prevent the sample from air exposure. Regardless of the interference of the Kapton tape peak below 30° (Figure S2), the rest of the peaks correlate well with the reference peaks of Na_2CS_3. The broadened peaks indicate that even though the secondary particles are micron-sized, primary crystallites seem to be nano-sized Na_2CS_3. The disappearance of the Na_2S peaks reveals the complete conversion of the sulfides into trithiocarbonates. The thermal stability of the synthesized Na_2CS_3 is shown in Figure S3.

To investigate the chemistry and molecular structure of the Na_2CS_3, Fourier transform infrared (FTIR) spectroscopy was conducted (Figure 1c). Distinctive to Na_2S, the carbon-sulfur resonance bond stretching is reflected as a broad adsorption band at 820 – 930 cm^{-1}. The peak position correlates to the previously reported carbon-sulfur resonance bond of trithiocarbonates.[37,45] To further confirm the bonding environment surrounding the carbon nuclei, ^{13}C nuclear magnetic resonance (NMR) spectroscopy was employed. As shown in Figure 1d, the peak affiliated with the carbon-sulfur resonance bond appears at 207 ppm. A clear downfield shift is detected compared to the peak of CS_2 at 192 ppm, due to the decreased diamagnetic shielding effect expected from the heightened number of surrounding sulfur atoms. The chemical state of sulfur is revealed by X-ray photoelectron spectroscopy (XPS) in Figure 1e. Compared to the sulfide peak (S^{2-}) appearing at 159 eV, the carbon-sulfur resonance peak appears at 161.3 eV. The peak shift towards higher binding energy confirms the

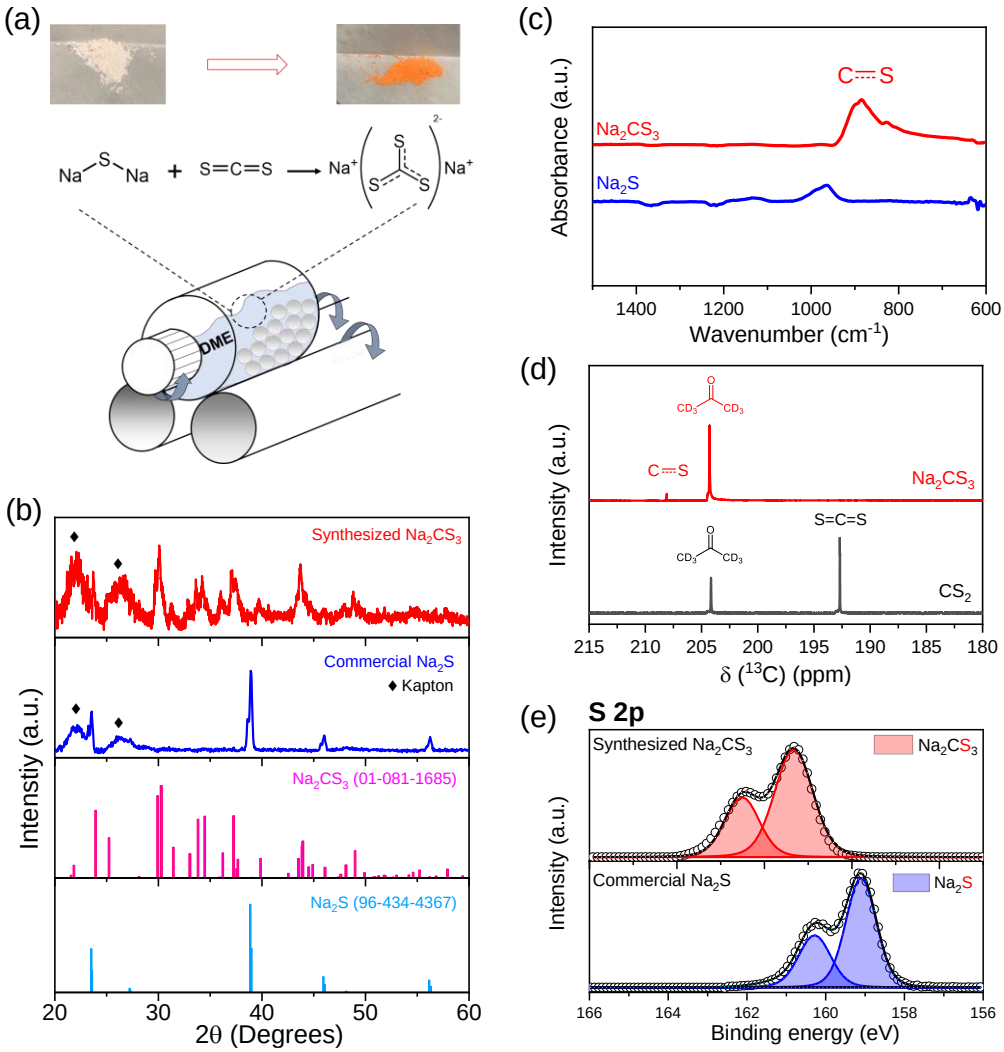

Figure 1. (a) Synthesis schematic of Na_2CS_3. (b) XRD patterns of synthesized Na_2CS_3, commercial Na_2S, reference peaks of Na_2CS_3, and reference peaks of Na_2S. (c) FTIR spectra of Na_2CS_3 and Na_2S. (d) ^{13}C NMR spectra of Na_2CS_3 and CS_2. (e) S 2p XPS data of synthesized Na_2CS_3 and commercial Na_2S.

oxidation of sulfur while forming Na_2CS_3. Hence, the series of materials characterization confirm the complete reaction of Na_2S and CS_2 to form Na_2CS_3.

Electrochemical cell performances

With a thorough understanding of the formation of Na_2CS_3 and its molecular structure, Na metal half cells were assembled and tested at a C/10 rate. The ether-based electrolyte, tetraethylene glycol dimethylether (TEGDME), was chosen since it is known to suffer from high solubility of long-chain polysulfides, severe shuttling effect, and failure to form stable SEI.[46–48] The active materials were dissolved in a DME solvent along with multi-walled carbon nanotubes (MWCNT) in a weight ratio of 7 : 3. This solution was drop-casted between two carbon papers and fully dried to be used as a binder-free cathode. Ceramic-coated separators were utilized to ensure sufficient wetting, and the cells were constructed in the form of Na ll Na_2CS_3 and Na ll Na_2S. An excess electrolyte amount (25 µL mg^{-1} with respect to active material) was injected to avoid additional variables of lean-electrolyte condition. The specific capacities were calculated based on the active material weight for the ease of comparison. The cells were charged up to 2.6 V and discharged down to 1.2 V, which will be discussed in detail in the later section.

Figure 2a shows the third cycle galvanostatic charge-discharge curves of Na ll Na_2CS_3 and Na ll Na_2S cells with an active material loading of 1.5 mg cm^{-2}. The discharge mechanism of Na-S is similar to Li-S but not identical, due to the intrinsic property differences between sodium and lithium, such as standard reduction potential (-2.71 V for Na and -3.04 V for Li vs. SHE), ionic radius, and reactivity. Similar to the previous reports in the literature,[49] the Na ll Na_2S cells show a conventional multi-step reduction reaction with an average discharge voltage of 1.79 V. At the high-discharge plateau region (2.31 – 2.20 V), highly soluble Na_2S_8 are produced. In the subsequent sloping region (2.20 – 1.68 V), they convert into less soluble Na_2S_4. In the low-discharge plateau (1.68 – 1.62 V), transitional products of insoluble Na_2S_3 and Na_2S_2 are formed,

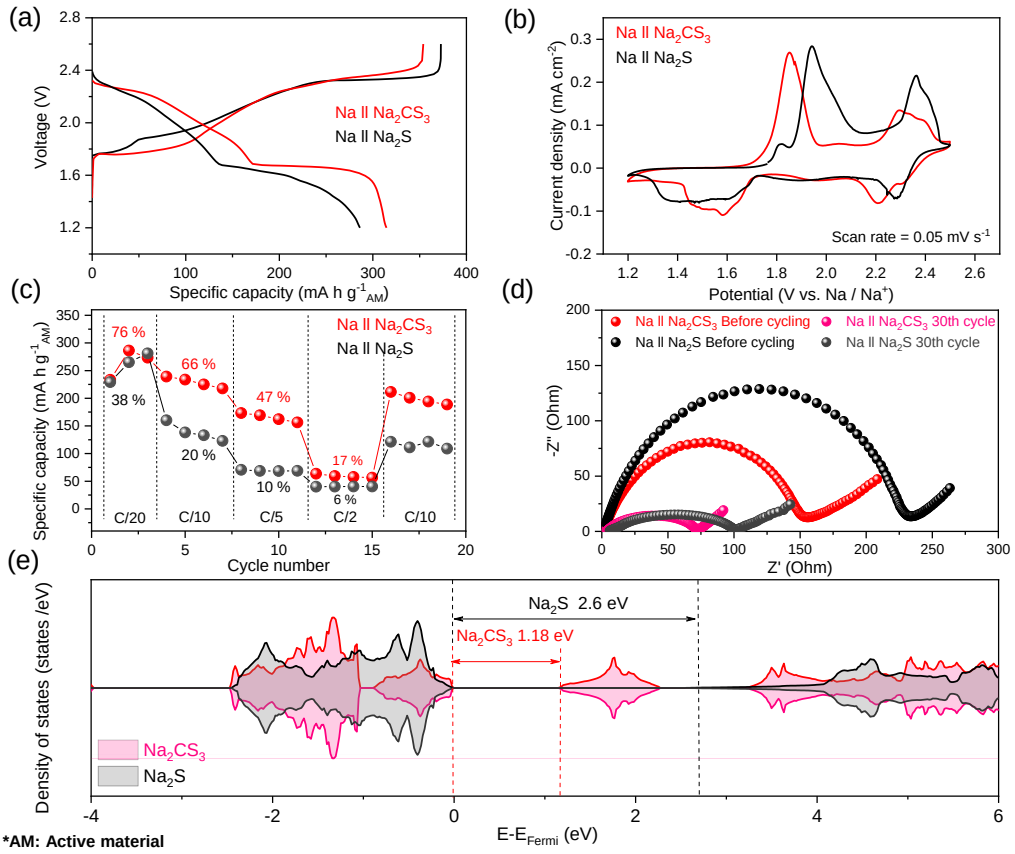

Figure 2. (a) Voltage curves of the Na ll Na_2CS_3 and Na ll Na_2S cells in the 3rd cycle with an active material loading of 1.5 mg cm^{-2}. (b) CV curves of Na ll Na_2CS_3 and Na ll Na_2S cells. (c) Rate performance of Na_2CS_3 and Na_2S cathodes at various C rates. The percentage number corresponds to the active material utilization based on the theoretical capacity. All specific capacities are based on the active material loading. (d) Nyquist plots before and after 30 cycles. (e) Total electronic density of states of Na_2CS_3 and Na_2S.

and the final sloping region (1.62 – 1.20 V) corresponds to the solid-solid conversion into Na_2S.

While the discharge curve of Na ll Na_2CS_3 cell shows an analogous two-plateaued trend, it exhibits a much higher average discharge voltage of 1.88 V. The high-discharge plateau becomes prominent at a voltage of ~ 2.28 V, and the sloping region (2.28 – 1.68 V) is shifted towards a higher potential compared to the Na_2S cathode. The low-discharge plateau at 1.68 V also becomes more noticeable with an enhanced total discharge capacity of 314 mA h g^{-1} compared to the control cell (285 mA h g^{-1}). It is expected that the different molecular coordination of Na_2CS_3 alters the conventional sulfur reaction pathway and shifts the discharge voltage curve. Furthermore, there are significant differences in the charge profiles. Specifically, much less overpotential is detected on the lower-charge plateau (1.88 V for Na_2S and 1.75 V for Na_2CS_3). The reduced polarization between charge and discharge curves signifies that the reaction of Na_2CS_3 might be kinetically more favorable compared to that of Na_2S.

Cyclic voltammetry (CV) curves of the Na ll Na_2CS_3 and Na ll Na_2S cells (Figure 2b) show consistent results with the voltage curves. Na ll Na_2S cells show an upper cathodic peak at 2.29 V and a broad lower cathodic peak centered at 1.47 V, whereas Na ll Na_2CS_3 cells show two sharp cathodic peaks at 2.21 and 1.56 V. Further, it is clearly shown that the anodic peaks of Na ll Na_2CS_3 cells get shifted towards lower potentials compared to Na ll Na_2S cells. From the voltage profiles and CV curves, it is observed that the altered reaction pathway of Na_2CS_3 leads to both a reduced polarization and higher total capacity.

The reduced polarization at the early stages of the cell cycling can be attributed to the enhanced reaction kinetics of the cathode. To verify this hypothesis, galvanostatic charge / discharge at various current rates were evaluated in Figure 2c. The Na ll Na_2CS_3 cells achieved an average capacity of 264, 229, 165, and 59 mA h g^{-1} at, respectively, C/20, C/10, C/5, and C/2 rates, which is much higher than those of the Na ll Na_2S cells (258, 139, 69, and 40 mA h g^{-1}). When the rate is recovered to C/10, the average capacity recovers back to 198 mA h g^{-1}, which indicates the superior rate performance and stability of the Na_2CS_3 cathode. It is important to note that Na_2CS_3 cathode displays an extremely high material utilization of 76 % (theoretical specific capacity of Na_2CS_3 is 348 mA h g^{-1}) at C/20 rate, whereas Na_2S cathode exhibits only 38 % utilization (theoretical specific capacity of Na_2S is 687 mA h g^{-1}). The remarkable material utilization and rate performance support the facile reaction kinetics of Na_2CS_3 cathode.

It is well accepted that conjugated structures facilitate electron transport process during the electrochemical reaction. Since the CS_3^{2-} anion contains carbon-sulfur resonance bond, which is highly conductive, delocalized electrons provide sufficient ionic and electronic pathways to maintain facile reaction kinetics, higher material utilization, and low resistance of the cell. Furthermore, the similar electronegativity between carbon (2.55) and sulfur (2.58) forms a covalent bond, which performs as a good electron conductor compared to the highly ionic Na2S cathode. The density of states calculation was conducted to compare the band gap of single molecule Na_2CS_3 and Na_2S. The narrower band gap of Na_2CS_3 (1.18 eV) rather than Na_2S (2.6 eV), as shown in Figure 2e, well supports the highly conductive nature of Na_2CS_3.

With a firm understanding of the facile electrochemical process taking place in Na_2CS_3, the cyclic stability of the cells at an active material loading of 1.5 mg cm^{-2} is compared. Surprisingly, as shown in Figure 3a, the Na ll Na_2CS_3 cells show a remarkable cycling performance improvement compared to the conventional Na ll Na_2S cells. The peak discharge capacity is 306 mA h g^{-1} on the active material basis, and a high capacity of 178 mA h g^{-1} is maintained (58 % retention) after 50 cycles. In addition, throughout the entire cycling process, the Na_2CS_3 cathode shows a higher coulombic efficiency than the Na_2S cathode, indicating that the trithiocarbonate-based cathode material effectively mitigates the polysulfide shuttle effect. In contrast, the conventional Na_2S cathode delivers a peak discharge capacity of 300 mA h g^{-1} and experience the sharp capacity decay to 82 mA h g^{-1} (27 % retention). The rapid capacity drop is mainly caused by the severe shuttling effect of polysulfides in the glyme-based electrolytes.[50]

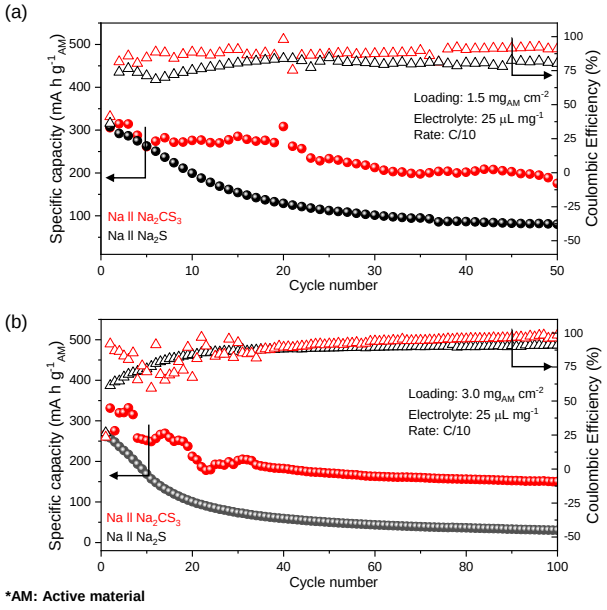

Figure 3. Cycling performances of half cells with Na_2CS_3 cathode (red) and Na_2S cathode (black) at an active material loading of (a) 1.5 mg cm^{-2} and (b) 3.0 mg cm^{-2}.

To further improve the energy density, cells with a higher active material loading of 3.0 mg cm^{-2} were also tested. As shown in Figure 3b, the Na_2CS_3 cathode still outperforms (151 mA h g^{-1}, 55 % retention) the conventional Na_2S cathode (34 mA h g^{-1}, 14% retention) at the end of 100 cycles. At a high loading, the discharge capacity and coulombic efficiency of Na ll Na_2CS_3 cells become unstable at the early stages of cycling, which might be mainly due to the formation of an interphase layer between the electrodes and the electrolyte. The prolonged cycling stability and enhanced coulombic efficiency of Na_2CS_3 cathode signify that trithiocarbonates are an attractive cathode material for RT Na-S batteries. Now, how Na_2CS_3 contributes to the improvement in the cell performance needs to be investigated in detail and understood.

Reaction mechanisms and suppressed active material dissolution of Na_2CS_3

To unveil the reaction mechanisms of Na_2CS_3 and its contribution to the cell performance improvement, XPS analysis was conducted on the cathode at different stages of charge (Figure 4a). When the pristine Na ll Na_2CS_3 cells are charged up to 2.2 V, the S $2p_{3/2}$ peak at 162.9 eV emerges, which represents the C = S bond.[51] Small peaks detected beyond 166 eV are coming from the thiosulfate and sulfate complexes originating from the oxidized sulfide species.[52,53] On the cell charged up to 2.4 and 2.6 V, the constant attenuation of the carbon-sulfur resonance bond (161.3 eV) and increment of the C = S bond is observed. During the de-sodiation process, it is explored that the intermediate products start to form the [-CS_3-CS_3-] oligomer-like compounds, as shown in Schematic 1. Interestingly, when the cell is charged up to 2.8 V, a sudden increase in the peak of sulfate complexes is detected. It is assumed at this potential, severe electrolyte and salt decomposition is triggered with the presence of an intermediate charged product of Na_2CS_3.

The SEM image of the electrode reveals well the charging process of Na_2CS_3, as shown in Figure S4. At the early stages of charge (2.2 V), the electrode is mainly covered with sharp-edged Na_2CS_3. Upon charging (2.4 V), the transformation from carbon-sulfur resonance bond to C = S is taking place at the boundaries of Na_2CS_3, and the sharp edges start to become blunt. At 2.6 V, most of the surface material got transformed into C = S containing species whereas at 2.8 V, the electrode is suddenly covered with the electrolyte and salt decomposed products. The SEM image provides well the visual image of active material transformation and electrolyte / salt decomposition upon cell charge, which correlates to the XPS data. The effect of the electrolyte and salt decomposition when charging the cells up to 2.8 V is examined in Figure S5. A sharp capacity decay within 3 cycles is observed when the Na ll Na_2CS_3 cells are charged up to 2.8 V, whereas a stable cycling performance is shown when the cells are charged to 2.6 V. It is expected that the irreversible reactions between Na_2CS_3 species and the electrolyte take place above 2.6 V, resulting in a fast

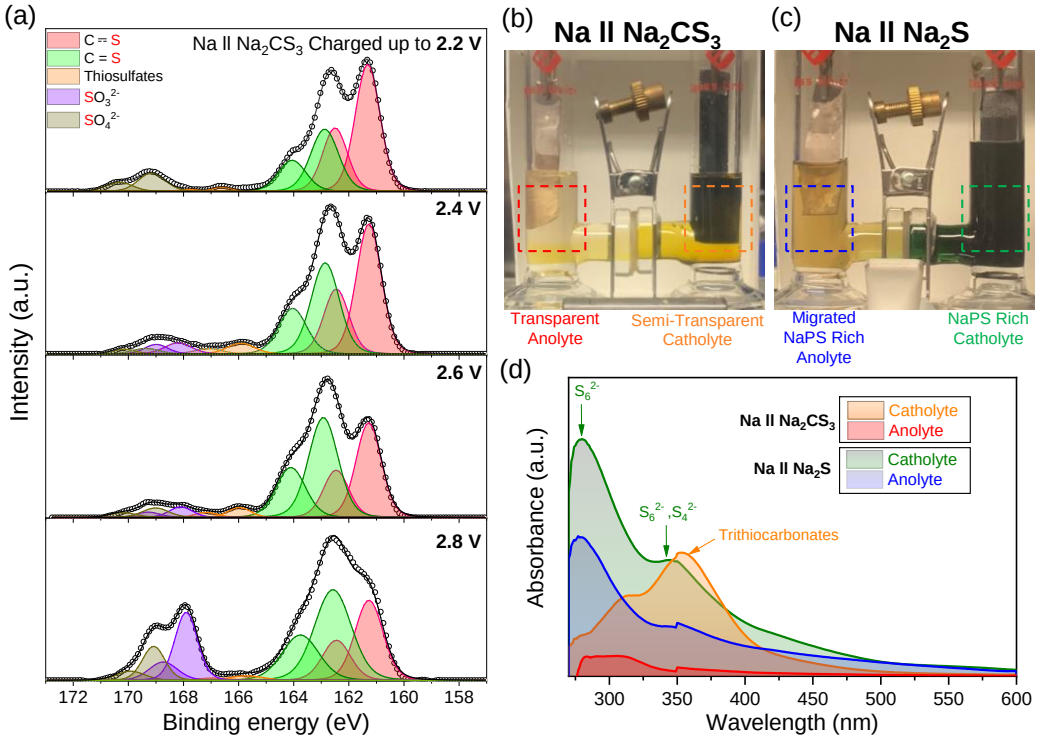

Figure 4. (a) S 2p XPS data of Na_2CS_3 cathode charged up to different states. Image of optical H-cells after a single charge and discharge: (b) Na ll Na_2CS_3 and (c) Na ll Na_2S cells. (d) UV-visible spectra of the catholytes and anolytes of Na ll Na_2CS_3 and Na ll Na_2S H-cells. Electrolytes were collected at the discharged state.

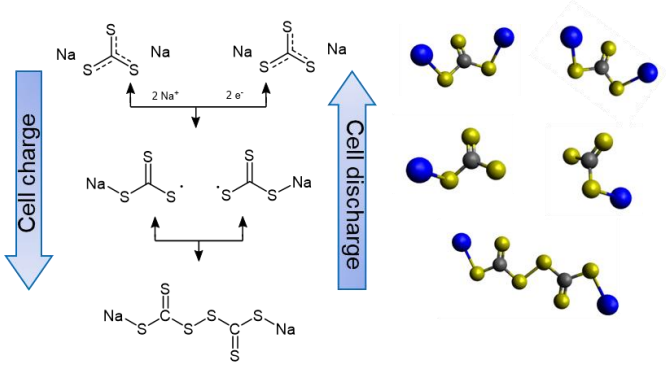

Schematic 1: Reaction mechanism of Na_2CS_3 during charge and discharge.

capacity decay. To avoid this type of reaction, all the electrochemical cells were charged only up to 2.6 V.

It is also worthwhile to explore how the [-CS_3-CS_3-] oligomer layers formed upon charge can improve the cell cycling performance. Compared to the sodium polysulfides, the oligomer structured Na_2CS_3 compounds might have heavier molar mass and bulky structure. This could prevent the dissolution and migration of the active materials, thus effectively inhibiting the shuttling of active materials. The effect of Na_2CS_3 preventing the active material dissolution is evidenced by the optical H-type electrochemical cell. The Na-metal anode was combined with Na_2CS_3 and Na_2S cathode and galvanostatically cycled inside an argon-filled glovebox. As shown in Figure 4b, the Na_2CS_3 cathode exhibit a semi-transparent yellow catholyte after a single charge and discharge step due to the suppressed active material dissolution. Transparent anolyte and fresh sodium-metal surface correspond to the mitigated shuttle effect. In contrast, the Na_2S cathode in Figure 4c shows a severe dissolution and diffusion of sodium polysulfides with obvious catholyte color change into the opaque green. The color of dissolved sodium polysulfides in TEGDME is known to be green, as previously reported.[54] The anolyte became semi-transparent orange and the discoloration of sodium metal surface was detected, which clearly reveals the parasitic side reaction of Na metal and migrated sodium polysulfides taking place at the surface. The optical H-cell qualitatively confirms the prominent suppression of active-material dissolution and shuttle effect of the Na_2CS_3 cathode.

To quantitatively measure the dissolved active materials in the electrolyte from the optical H-cell, Ultraviolet-visible (UV-Vis) spectroscopy was conducted. Figure S6a shows the UV-Vis absorption spectra of electrolytes at the charged and discharged states of the H-cell, when using Na_2CS_3 as a cathode. During the initial charge of the cell, negligible amount of active material gets dissolved into both the catholyte and anolyte. The subsequent discharging step reveals some amount of active material dissolution into the catholyte. The broad peak at 300 – 400 nm region corresponds to the intermediate oligomer structured trithiocarbonate species.[55] It is important to note that the anolyte still shows no peaks, which indicates that the intermediate Na_2CS_3 species barely diffuse into the anode side.

In contrast, Figure S6b demonstrates the high absorbance of polysulfide peaks in both catholyte and anolyte when using Na_2S as a cathode. The peak at 280 nm represents

the long chain polysulfides (S_6^{2-}), which aligns with the synthesized Na_2S_6 peak shown in Figure S7. The broad band at 350 – 400 nm corresponds to S_4^{2-} and S_6^{2-}, which exhibits the co-existence of multiple forms of polysulfides in equilibrium.[48,56] The high intensity of polysulfide signals at both catholyte and anolyte exhibit severe sodium polysulfide dissolution and migration throughout the cell cycling. Figure 4d compares the absorption spectra of Na_2CS_3 and Na_2S cathode at its discharged state in a single plot. It is clearly observed that the oligomer-structured Na_2CS_3 intermediates prominently hamper active material dissolution and shuttle effect compared to the conventional Na_2S cells. These H-cell and UV-Vis data are consistent with the cycling data, showing that Na_2CS_3 cathode performs with superior coulombic efficiency.

Sodium-metal anode morphology and SEI chemistry

It is necessary to further investigate the effect of Na_2CS_3 on the Na-metal anode side. The Na ll Na_2CS_3 and Na ll Na_2S cells after 20 cycles were disassembled, and the Na metal was rinsed with TEGDME solvent. The macroscopic morphology of the Na metal was compared based on their optical photographs. Surprisingly, as shown in Figure S8, Na-metal anode paired with Na_2CS_3 cathode still maintains the shiny surface with a partial presence of discolored spots. In contrast, Na metal assembled with Na_2S cathode shows a thick discolored layer covering the entire surface. The detailed microscopic morphology of the Na-metal anode was investigated with SEM. As shown in Figure 5a, smooth and non-dendritic growth behavior is detected in the Na metal combined with the Na_2CS_3 cathode. It might be the consequence of stable SEI layer formation in the presence of Na_2CS_3, which protects well the Na metal from side reactions and helps improve the sodium stripping and plating performance. In contrast, the Na metal assembled with the Na_2S cathode, exhibits bumpy and porous surface morphology (Figure 5b). Such irregular growth of Na metal led to severe side reactions with electrolytes and

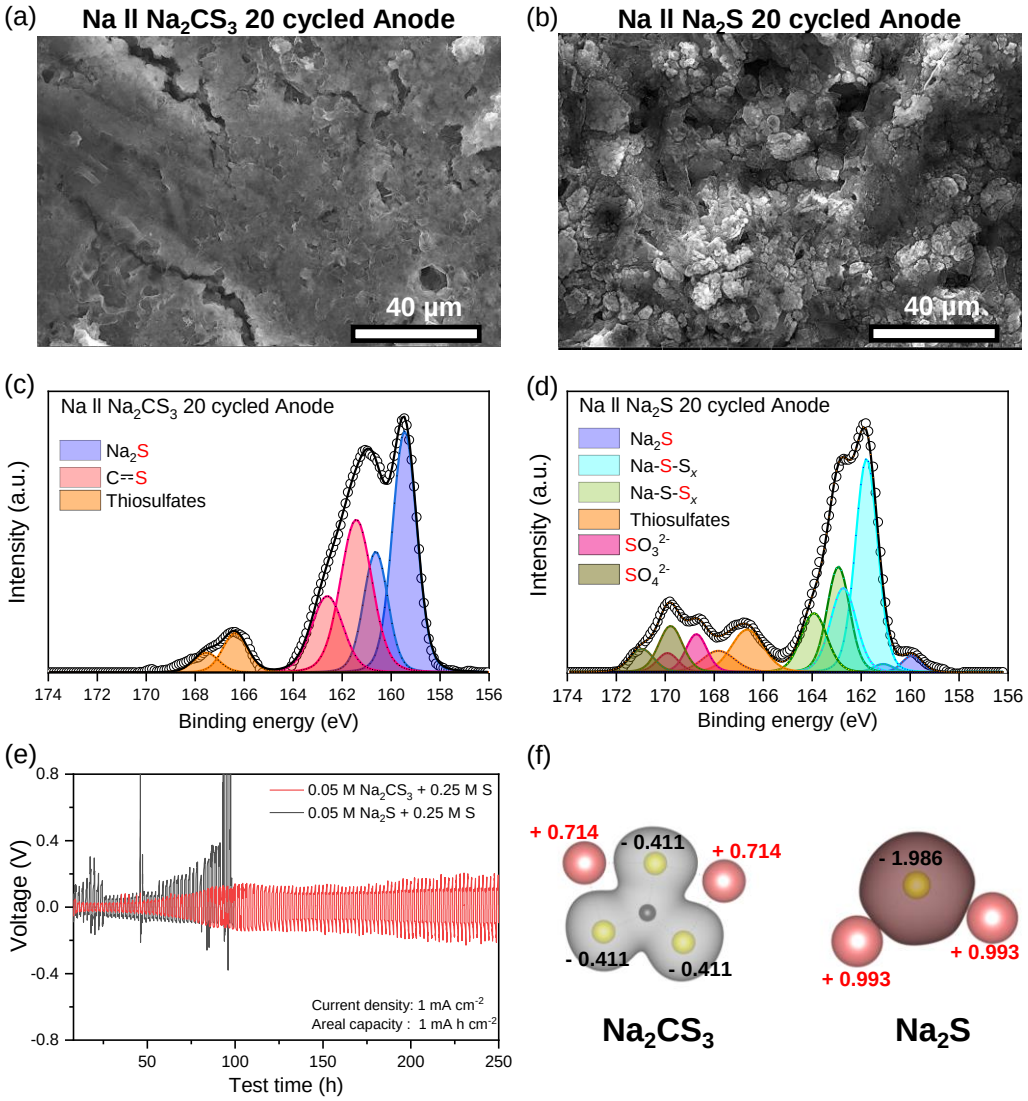

Figure 5. SEM image of Na-metal anode after 20 cycles: (a) Na ll Na_2CS_3 and (b) Na ll Na_2S cells. S 2p XPS data of Na-metal anode after 20 cycles: (c) Na ll Na_2CS_3 and (d) Na ll Na_2S cells. (e) Cycling stability of Na ll Na symmetric cells with polysulfide form of Na_2CS_3 and Na_2S_6. (f) Bader charge analysis of Na_2CS_3 and Na_2S.

polysulfides, which causes a depletion of the electrolyte and consumption of the active materials.

To gain insights into the homogeneous Na-metal anode morphology in presence of Na_2CS_3, XPS analysis was employed to understand the chemical composition of the surface of the SEI layer. Interestingly, the major component of the SEI layer in the Na ll Na_2CS_3 cell turns out to be a reduced sulfur species of S^{2-} from Na_2S (159.5 eV) and carbon-sulfur resonance bond from Na_2CS_3 (161.3 eV) (Figure 5c). A small intensity of thiosulfates (166.3 eV) signifies the minimized side reactions of Na metal with the electrolyte, owing to the uniform morphology of sodium with low surface area. To further identify the species in the bulk of the deposited sodium metal, Ar^+ sputtering was conducted. In general, the surface of the SEI layer may not have a complete reduction of the material due to the limited access to metallic Na and electron conduction pathways. However, such a kinetic hindrance will be attenuated in the bulk side of sodium metal, so a more severe reducing condition could be fostered in the bulk side of sodium metal. Figure S9 shows the S 2p XPS data after sputtering the surface for 10 mins (~ 250 nm of material removal), and the carbon-sulfur resonance bond is still detected at 161.3 eV. This implies that the trithiocarbonates are stable toward reduction, which makes them an ideal SEI component. In sharp contrast, the SEI layer of the Na ll Na_2S cell is dominated by the sodium polysulfide signals of bridging sulfur (163 eV) and terminal sulfur species (161.9 eV). The high intensity of the oxidized sulfur species, such as thiosulfates, SO_3^{2-} (168.6 eV), and SO_4^{2-} (169.8 eV), indicates the reactive Na metal undergoing severe side reactions with the electrolyte, which implies it does not form a stable SEI layer.

From the cycled Na-metal anode analysis, it is confirmed that the inclusion of Na_2CS_3 in the system clearly induces a homogenous Na metal morphology and forms a unique carbon-sulfur resonance bond containing SEI layer. Also, from the previous section, the effective inhibition of polysulfide shuttling from the Na_2CS_3 cathode has been verified. It is widely known that the parasitic reactions between corrosive Na metal and migrated polysulfides lead to a complex, unstable, and fragile SEI layer that causes roughened Na deposition. Now it is important to clarify if the improved Na metal surface morphology is solely the consequence of the suppressed polysulfide shuttling, or the formation of unique carbon-sulfur resonance bond containing SEI layer is also contributing to the enhanced stripping and plating performance.

To answer this question, long-term cycling stability of Na ll Na symmetric cells was tested at a current density of 1 mA cm^{-2} and an areal capacity of 1 mA h cm^{-2}. The 0.05 M polysulfide form of Na_2CS_3 and Na_2S were dissolved into the electrolyte. As shown in Figure 5e, the cell containing the polysulfide form of Na_2CS_3 shows a much lower initial overpotential (27 mV) compared to the conventional sodium polysulfides (86 mV) at the early stages of cycling. The voltage hysteresis gradually increases to 110 mV until 80 h, and maintains its overpotential values for more than 250 h. However, the cell including conventional sodium polysulfides shows a sudden increase in overpotential after 60 h. It showed cell failure at around 100 h, indicating unstable SEI formation and dendritic growth of sodium. The Na ll Na symmetric cell experiment demonstrates that the cell polarization can be greatly reduced by introducing Na_2CS_3 compounds into the system. Generally, the reduced voltage hysteresis and stable cycle life of Na ll Na symmetric cells are due to the formation of favorable Na-ion conducting SEI layer, suppressing dendritic growth of Na. Thus, it has been proven that the homogeneous morphology of Na-metal anode and prolonged cycle life are not only the consequence of the suppressed shuttle effect, but also due to the formation of a unique, stable SEI layer. The result is in good agreement with the previous report that trithiocarbonates can act as a SEI modifying agent to enhance the Li morphology in Li-ion batteries.[35]

To understand the underlying mechanism of Na_2CS_3, including the SEI layer showing the enhanced stripping and plating performance, first-principle density functional theory (DFT) calculation was conducted. Bader charge analysis shown in Figure 5f reveals an electron density spread on Na_2CS_3 and Na_2S molecules. For ternary sulfides (Na_2CS_3), which contains the carbon-sulfur resonance bonds, the covalent characteristic between carbon and sulfur bond effectively spreads the electron density. Consequently, the sulfur atom, which is constituent with the most electron density in the molecule, only contains a net electron charge of – 0.411. The positively charged Na ions might experience a low diffusion barrier when traveling through the Na_2CS_3-rich SEI layer. This can facilitate a homogeneous and facile Na-ion flux without local charge accumulation. In contrast, the binary Na_2S and other sodium polysulfides (Figure S10), which are the main SEI components of the conventional Na ll Na_2S cells, have a highly ionic bond characteristic due to the large electronegativity difference between Na (0.93) and S (2.58). The sulfur atom in Na_2S possesses a high electron density, resulting in a net electron charge of -1.986. The terminal sulfur of Na_2S_2 and Na_2S_4 sodium polysulfides also showed a high electron charge of -0.706 and -0.612. The locally concentrated charge causes an uneven electric field and Na-ion flux, leading to poor inhomogeneous Na deposition. The Bader charge analysis provides a good explanation of a Na_2CS_3-containing SEI layer promoting a uniform and dense morphology of the Na metal surface, minimizing the reaction sites of corrosive sodium with electrolytes and polysulfides.

Conclusions

In summary, we have shown that the trithiocarbonates applied as a cathode material in RT Na-S batteries enable a multi-functional improvement to the cell performance, both from a reaction kinetics standpoint and from a cycling stability perspective. Owing to its conjugate structure and highly covalent characteristic, Na_2CS_3 enables efficient active material

utilization and superior rate performance compared to the Na_2S cathode. From a standpoint of cell cyclability improvement, Na_2CS_3 is used to modulate both the cathode and the anode dynamics. It is recognized that the [-CS_3-CS_3-] oligomer structures are formed at the cathode during cell cycling, which suppresses active material dissolution and shuttling. Furthermore, a unique carbon-sulfur resonance bond containing SEI layer is formed on Na-metal anode surface, which enables a uniform Na-ion flux. Consequently, the Na_2CS_3 cathode displays a higher average discharge voltage (1.88 V) compared to the Na_2S cathode (1.79 V) with lower charge-transfer resistance and cell polarization. An outstanding active material utilization of 76 % is realized, while Na_2S shows only 38 % utilization at C/20 rate. In the well-designed Na ll Na_2CS_3 cells, a superior cycling performance is achieved with an active material loading of 1.5 mg cm^{-2} (58 % retention over 50 cycles) and 3.0 mg cm^{-2} (55 % retention over 100 cycles). This work provides a rational cathode design strategy to realize high-energy density long cycle life RT Na-S batteries.

Conflicts of interest

The authors declare no competing financial interest.

Acknowledgements

This work was supported by the U.S. Department of Energy, Office of Basic Energy Sciences, Division of Materials Science and Engineering under award number DE-SC0005397.

References

1 A. Manthiram, *Nat. Commun*., 2020, **11**, 1550.
2 A. Manthiram, *J. Phys. Chem. Lett*., 2011, **2**, 176–184.
3 B. Scrosati and J. Garche, *J. Power Sources*, 2010, **195**, 2419–2430.
4 A. Manthiram, A. Vadivel Murugan, A. Sarkar and T. Muraliganth, *Energy Environ. Sci.,* 2008, **1**, 621–638.
5 A. Manthiram, *ACS Cent. Sci*., 2017, **3**, 1063.
6 X. Yu and A. Manthiram, *Adv. Funct. Mater*., 2020, **30**, 2004084.
7 D. Lide, *CRC Handbook of Chemistry and Physics 85th ed*, 2004
8 A. Manthiram and X. Yu, *Small*, 2015, **11**, 2108–2114.
9 B. Dunn, H. Kamath and J. M. Tarascon, *Science*., 2011, **334**, 928–935.
10 Z. Yang, J. Zhang, M. C. W. Kintner-Meyer, X. Lu, D. Choi, J. P. Lemmon and J. Liu, *Chem. Rev*., 2011, **111**, 3577–3613.
11 N. Tanibata, M. Deguchi, A. Hayashi and M. Tatsumisago, *Chem. Mater.,* 2017, **29**, 5232–5238.
12 C. W. Park, J. H. Ahn, H. S. Ryu, K. W. Kim and H. J. Ahn, *Electrochem. Solid-State Lett*., 2006, **9**, A123-A125.
13 Y. Wang, Y. Zhang, H. Cheng, Z. Ni, Y. Wang, G. Xia, X. Li and X. Zeng, *Mol. 2021*, **26**, 1535
14 H. Liu, W.-H. Lai, Y. Lei, H. Yang, N. Wang, S. Chou, K. Liu, S. X. Dou, Y.-X. Wang, H. Liu, W.-H. Lai, Y. Lei, H. Yang, N. Wang, S. Chou, H. K. Liu, S. X. Dou and Y.-X. Wang, *Adv. Energy Mater*., 2022, **12**, 2103304.
15 W. Du, Y. Wu, T. Yang, B. Guo, D. Liu, S. J. Bao and M. Xu, *Chem. Eng. J.,* 2020, **379**, 122359.
16 X. Yu and A. Manthiram, *J. Phys. Chem. Lett.,* 2014, **5**, 1943–1947.
17 Y. M. Chen, W. Liang, S. Li, F. Zou, S. M. Bhaway, Z. Qiang, M. Gao, B. D. Vogt and Y. Zhu, *J. Mater. Chem. A*., 2016, **4**, 12471–12478.
18 N. Chawla and M. Safa, *Electron*., 2019, **8**, 1201.
19 B. W. Zhang, Y. D. Liu, Y. X. Wang, L. Zhang, M. Z. Chen, W. H. Lai, S. L. Chou, H. K. Liu and S. X. Dou, *ACS Appl. Mater. Interfaces*., 2017, **9**, 24446–24450.
20 N. Wang, Y. Wang, Z. Bai, Z. Fang, X. Zhang, Z. Xu, Y. Ding, X. Xu, Y. Du, S. Dou and G. Yu, *Energy Environ. Sci*., 2020, **562**, 562–570.
21 D. Ma, Y. Li, J. Yang, H. Mi, S. Luo, L. Deng, C. Yan, M. Rauf, P. Zhang, X. Sun, X. Ren, J. Li and H. Zhang, *Adv. Funct. Mater*., 2018, **28**, 1705537.
22 W. Bao, C. E. Shuck, W. Zhang, X. Guo, Y. Gogotsi and G. Wang, *ACS Nano*, 2019, **13**, 11500–11509.
23 H. Liu, W. Pei, W. H. Lai, Z. Yan, H. Yang, Y. Lei, Y. X. Wang, Q. Gu, S. Zhou, S. Chou, H. K. Liu and S. X. Dou, *ACS Nano*, 2020, **14**, 7259–7268.
24 Z. Yan, J. Xiao, W. Lai, L. Wang, F. Gebert, Y. Wang, Q. Gu, H. Liu, S. L. Chou, H. Liu and S. X. Dou, *Nat. Commun.,* 2019, **10**, 4793
25 B. W. Zhang, T. Sheng, Y. D. Liu, Y. X. Wang, L. Zhang, W. H. Lai, L. Wang, J. Yang, Q. F. Gu, S. L. Chou, H. K. Liu and S. X. Dou, *Nat. Commun*., 2018, **9**, 4082
26 B. W. Zhang, S. Li, H. L. Yang, X. Liang, W. H. Lai, S. Zhao, J. Dong, S. Q. Chu, Q. F. Gu, J. Liang, Y. Du, X. Xu, L. Cao, Y. X. Wang, F. Pan, S. L. Chou, H. K. Liu and S. X. Dou, *Cell Reports Phys. Sci*., 2021, **2**, 100531.
27 X. Zhang, A. Wang, X. Liu and J. Luo, *Acc. Chem. Res*., 2019, **52**, 3223–3232.
28 Y. He, X. Ren, Y. Xu, M. H. Engelhard, X. Li, J. Xiao, J. Liu, J. G. Zhang, W. Xu and C. Wang, *Nat. Nanotechnol.,* 2019, **14**, 1042–1047.
29 S. Wei, S. Choudhury, J. Xu, P. Nath, Z. Tu and L. A. Archer, *Adv. Mater*., 2017, **29**, 1605512.
30 V. Kumar, A. Y. S. Eng, Y. Wang, D. T. Nguyen, M. F. Ng and Z. W. Seh, *Energy Storage Mater*., 2020, **29**, 1–8.
31 S. Choudhury, S. Wei, Y. Ozhabes, D. Gunceler, M. J. Zachman, Z. Tu, J. H. Shin, P. Nath, A. Agrawal, L. F. Kourkoutis, T. A. Arias and L. A. Archer, *Nat. Commun*., 2017, **8**, 898–898.
32 X. Zheng, H. Fu, C. Hu, H. Xu, Y. Huang, J. Wen, H. Sun, W. Luo and Y. Huang, *J. Phys. Chem. Lett.,* 2019, **10**, 707–714.
33 Y. Lee, J. Lee, J. Lee, K. Kim, A. Cha, S. Kang, T. Wi, S. J. Kang, H. W. Lee and N. S. Choi, *ACS Appl. Mater. Interfaces*, 2018, **10**, 15270–15280.
34 Q. Shi, Y. Zhong, M. Wu, H. Wang and H. Wang, *Angew. Chemie Int. Ed.,* 2018, **57**, 9069–9072.
35 Y. Ein-Eli, *J. Electroanal. Chem*., 2002, **531**, 95–99.
36 Y. Chu, X. Cui and Q. Pan, *ACS Appl. Energy Mater.*, 2018, **1**, 6919–6926.
37 H. Sul, A. Bhargav and A. Manthiram, *Adv. Energy Mater.*, 2022, 2200680.
38 J. P. Perdew, K. Burke and M. Ernzerhof*, Phys. Rev. Lett*., 1996, **77**, 3865–3868.
39 J. J. Mortensen, L. B. Hansen and K. W. Jacobsen, *Phys. Rev. B,* 2005, **71**, 035109.
40 M. Thomas, D. Zdebik and B. Białecka, *Polish J. Environ. Stud*., 2018, **27**, 1753–1763.
41 M. Thomas, V. Kozik, A. Bąk, K. Barbusiński, J. Jazowiecka-rakus and J. Jampilek, *Materials (Basel).,* 2021, **14**, 1.

42 B. D. Stone, M. L. Nielsen, US Pat., 2893835A, 1959.
43 S. Perrier, P. Takolpuckdee, *J. Polym. Sci. Part A Polym. Chem.* 2005, **43**, 5347.
44 C. M. James, PhD thesis, University of Cologne, 2021.
45 H. Seidel and R. Meyn, Zeitschrift fur Naturforsch. - *Sect. B J. Chem. Sci.,* 1971, **26**, 1192.
46 L. Wang, T. Wang, L. Peng, Y. Wang, M. Zhang, J. Zhou, M. Chen, J. Cao, H. Fei, X. Duan, J. Zhu and X. Duan, *Natl. Sci. Rev*., 2021
47 X. Yu and A. Manthiram, *J. Phys. Chem. Lett.,* 2014, **5**, 1943–1947.
48 J. Pampel, S. Dörfler, H. Althues and S. Kaskel, *Energy Storage Mater.*, 2019, **21**, 41–49.
49 X. Yu and A. Manthiram, *Chem. – A Eur. J.,* 2015, **21**, 4233–4237.
50 D. Liu, Z. Li, X. Li, X. Chen, Z. Li, L. Yuan and Y. Huang*, ACS Appl. Mater. Interfaces*, 2022, **14**, 6658–6666.
51 A. Bhargav and A. Manthiram, *Adv. Energy Mater*., 2020, **10**, 2001658.
52 X. Liang, C. Hart, Q. Pang, A. Garsuch, T. Weiss and L. F. Nazar, *Nat. Commun*., 2015, **6**, 1–8.
53 S. Wei, S. Xu, A. Agrawral, S. Choudhury, Y. Lu, Z. Tu, L. Ma and L. A. Archer, *Nat. Commun*., 2016, **7**, 1–10.
54 I. Kim, J.-Y. Park, C. Kim, J.-W. Park, J.-P. Ahn, J.-H. Ahn, K.-W. Kim and H.-J. Ahn, *J. Electrochem. Soc.*, 2016, **163**, A611–A616.
55 J. A. Venter, PhD thesis, University of Pretoria, 2007
56 X. Yu and A. Manthiram, *Adv. Energy Mater.,* 2015, **5**, 1500350.